NANO · MICRO small
www.small-journal.com

Emitting/Sensitizing Ions Spatially Separated Lanthanide Nanocrystals for Visualizing Tumors Simultaneously through Up- and Down-Conversion Near-Infrared II Luminescence In Vivo

*Yingying Li, Peisen Zhang, Haoran Ning, Jianfeng Zeng, Yi Hou, Lihong Jing, Chunyan Liu, and Mingyuan Gao**

Near-infrared lights have received increasing attention regarding imaging applications owing to their large tissue penetration depth, high spatial resolution, and outstanding signal-to-noise ratio, particularly those falling in the second near-infrared window (NIR II) of biological tissues. Rare earth nanoparticles containing Er^{3+} ions are promising candidates to show up-conversion luminescence in the first near-infrared window (NIR I) and down-conversion luminescence in NIR II as well. However, synthesizing particles with small size and high NIR II luminescence quantum yield (QY) remains challenging. Er^{3+} ions are herein innovatively combined with Yb^{3+} ions in a $NaErF_4$@$NaYbF_4$ core/shell manner instead of being codoped into $NaLnF_4$ matrices, to maximize the concentration of Er^{3+} in the emitting core. After further surface coating, $NaErF_4$@$NaYbF_4$@$NaYF_4$ core/shell/shell particles are obtained. Spectroscopy studies are carried out to show the synergistic impacts of the intermediate $NaYbF_4$ layer and the outer $NaYF_4$ shell. Finally, $NaErF_4$@$NaYbF_4$@$NaYF_4$ nanoparticles of 30 nm with NIR II luminescence QY up to 18.7% at room temperature are obtained. After covalently attaching folic acid on the particle surface, tumor-specific nanoprobes are obtained for simultaneously visualizing both subcutaneous and intraperitoneal tumor xenografts in vivo. The ultrahigh QY of down-conversion emission also allows for visualization of the biodistribution of folate receptors.

1. Introduction

Near-infrared lights, particularly those falling in the second near-infrared window (NIR II, between ≈1000 and 1700 nm) of biological tissues (e.g., skin, fat, blood, etc.), exhibit a number of remarkable advantages over visible lights with respect to medical imaging applications,[1] including substantially improved tissue penetration depth and spatial resolution, and greatly enhanced signal-to-noise ratio, etc., owing to the remarkably reduced autofluorescence and light scattering.[2] All these advantages persist even compared with the lights in the first NIR window (NIR I, approximately from 650 to 950 nm).[3] In the past few years, great efforts have therefore been dedicated to developing NIR II imaging probes with small molecule dyes,[4] semiconductor quantum dots,[5] single-walled carbon nanotubes,[6] aggregation-induced emission luminogens,[7] conjugated polymers,[8] and lanthanide-based nanoparticles.[9] Among all these candidates, rare-earth nanoparticles exhibit remarkable characteristics suitable for biomedical applications, such as long luminescence lifetime, high photostability, and sharp emission peak, benefited from the unique electronic configurations of $4f^n$ (n = 0–14).[9b,10] For example, Nd^{3+} ions exhibit three NIR emission bands centered at around 900, 1060, and 1340 nm, respectively, upon 808 nm laser excitation.[11] Taking the advantage of these emissions, Ren et al. successfully visualized the vasculatures of tumors at different stages with $NaYF_4$:Nd@$NaGdF_4$ nanoparticles.[12] Different from Nd^{3+} ions, Er^{3+} ions present a longer wavelength

Y. Y. Li, P. S. Zhang, H. R. Ning, Dr. Y. Hou, Dr. L. H. Jing, Dr. C. Y. Liu, Prof. M. Y. Gao
Key Laboratory of Colloid
Interface and Chemical Thermodynamics
Institute of Chemistry
Chinese Academy of Sciences
Bei Yi Jie 2, Zhong Guan Cun, Beijing 100190, P. R. China
E-mail: gaomy@iccas.ac.cn
The ORCID identification number(s) for the author(s) of this article can be found under https://doi.org/10.1002/smll.201905344.

DOI: 10.1002/smll.201905344

Y. Y. Li, P. S. Zhang, H. R. Ning, Prof. M. Y. Gao
School of Chemistry and Chemical Engineering
University of Chinese Academy of Sciences
Beijing 100049, P. R. China
J. F. Zeng, Prof. M. Y. Gao
Center for Molecular Imaging and Nuclear Medicine
School for Radiological and Interdisciplinary Sciences (RAD-X)
Collaborative Innovation Center of Radiation Medicine of Jiangsu Higher Education Institutions, and State Key Laboratory of Radiation Medicine and Protection
Soochow University
Suzhou 215123, China

down-conversion emission peaking at 1525 nm under the same excitation, apart from 655 nm up-conversion emission in NIR I region. Although the 1525 nm emission slightly overlaps with the water bending overtone absorbance band at around 1450 nm, a virtual zero autofluorescence interference of tissues is expected owing to the further increased Stokes shift.[13] For example, the blood vessels of mice were clearly presented through the perfusion of β-$NaGdF_4$:Yb,Er@$NaYF_4$ core/shell nanoparticles,[14] while the NIR I up-conversion emission together with the visible emissions of $NaGdF_4$:Yb,Er@$NaGdF_4$ were adopted to image mouse orthotopic tumors in vivo.[15]

Nevertheless, most NIR II nanofluorophores reported so far are prepared by doping inert rare earth nanoparticles with Nd^{3+} or Er^{3+} emitters. Sometimes sensitizers, such as Yb^{3+} and Nd^{3+} ions, are also codoped to facilitate the absorption of 980 and 808 nm laser lights, respectively, for enhancing the luminescence through energy transfer between the sensitizer and emitter. Owing to the concentration quenching effect, low concentrations of sensitizer and emitter in particular are widely adopted for synthesizing luminescent lanthanide-doped rare earth nanocrystals,[16] typically below 20 and 2 mol%, respectively, which limits the luminescent brightness to a large extent.[17] Recently, Almutairi and co-workers found out that the intensity of the up-conversion luminescent Er^{3+}-doped $NaYF_4$ nanocrystal keeps increasing, while the concentration of Er^{3+} ions is raised from 5 to 100 mol%. But this tendency occurs only when the $NaYF_4$:Er particles are coated with $NaLuF_4$ shell, suggesting that surface quenching effect rather than the concentration quenching effect dominates the up- and down-conversion luminescence intensity.[18] Nevertheless, the absorption cross-section of Er^{3+} is very low, thereby effectively enhancing the absorption for better activating the f–f transitions becomes vital for further improving the NIR II luminescence of Er^{3+}. In fact, Yb^{3+} ion is widely used due to its large absorption cross-section at 980 nm to sensitize the up-conversion luminescence of Er^{3+}. But the effect of Yb^{3+} on the down-conversion luminescence of Er^{3+} remains rarely addressed. Moreover, Yb^{3+} ions are mainly codoped or blended with Er^{3+} ions in literature.[19] Therefore, innovatively combining Er^{3+} ions with Yb^{3+} ions to achieve particles with small size and high NIR II luminescence quantum yield (QY), and disclose the impacts of Yb^{3+} on both up- and down-conversion luminescence of Er^{3+} remains highly challenging and fundamentally interesting.

Following our previous investigations on the imaging applications of up-conversion nanoparticles,[20] herein we report our recent studies on the preparation, optical properties, and in vivo imaging applications of $NaErF_4$@$NaYbF_4$@$NaYF_4$ core/shell/shell nanocrystals simultaneously through their up- and down-conversion NIR II luminescence. By radially separating Er^{3+} and Yb^{3+}, high core concentrations of Er^{3+} ions and reduced surface quenching effect were rationally combined in $NaErF_4$@$NaYbF_4$ core/shell manner. In the meantime, the energy transfer process was expected to be better elucidated owing to the sensitizer/emitter spatial-separating design which was never reported before. Upon further growth of $NaYF_4$ shell, $NaErF_4$@$NaYbF_4$@$NaYF_4$ core/shell/shell particles showing improved near-infrared down- and up-conversion luminescence were obtained. Through surface ligand exchange and subsequent surface folic acid (FA) conjugation, a tumor specific probe was obtained, which allowed to combine the imaging capacities of up- and down-conversion luminescence of the same probe for sensitively visualizing both subcutaneously and intraperitoneally xenografted tumors and showing the detailed distribution of FA receptors across the entire tumorous regions as well.

2. Results and Discussions

2.1. Synthesis and Optical Properties of $NaYb_{0.5}Er_{0.5}F_4$ and $NaErF_4$@$NaYbF_4$ Nanocrystals

Differently structured $NaLnF_4$ nanoparticles were prepared, according to literature method,[21] through a high temperature approach using oleic acid as particle surface capping agent. To maximize the concentration of Er^{3+} emitters, $NaErF_4$ particles were directly synthesized instead of doping Er^{3+} in other matrix. As shown in **Figure 1**a, the as-prepared $NaErF_4$ particles are spherical and highly monodispersed with an average size of 15.6 ± 0.7 nm. To enhance the absorption of the excitation light, Yb^{3+} ions were adopted as sensitizer and combined with Er^{3+} in two different ways, i.e., forming a blended particle with Er^{3+} or forming a shell around the $NaErF_4$ cores. In the former structure, Er^{3+} and Yb^{3+} were simultaneously introduced into the reaction system to achieve a radially unseparated structure (denoted as $NaYb_{0.5}Er_{0.5}F_4$ according to the element contents in the final particles determined through inductively coupled plasma-atomic emission spectrometry (ICP-AES)); while in the latter particles, a $NaYbF_4$ shell was grown on preformed $NaErF_4$ cores to obtain a radially separated structure (denoted as $NaErF_4$@$NaYbF_4$). It should be mentioned that in both of these two particle samples, the contents of Er and Yb were kept identical. As shown in Figure 1b,c, the as-prepared $NaYb_{0.5}Er_{0.5}F_4$ nanoparticles are much larger than $NaErF_4$@$NaYbF_4$ core–shell nanoparticles, e.g., 62.3 ± 2.1 versus 23.0 ± 1.2 nm. In addition, the surface coating of $NaYbF_4$ shell (3.7 nm thick) did not broaden the particle distribution if comparing the core/shell particles with initial cores. The selected area electron diffraction (SAED) measurements, as shown in Figure S1 in the Supporting Information, revealed that all above nanoparticles were in hexagonal structure that is a favorable phase for luminescence, irrespective of the difference in particle size.

The optical properties of the above particles were then investigated. Due to the unique ladder-like energy levels of Er^{3+}, Er^{3+}-containing particles can in principle give rise to multiple emissions, e.g., 542 and 655 nm emissions in up-conversion luminescence and 1525 nm emission in down-conversion luminescence. As expected, $NaErF_4$ cores present all these emission lines under 980 nm excitation (Figure 1d), but with very low intensities. However, the emission intensities of both up- and down-conversion luminescence are remarkably increased by factors of 12.0 and 12.7, respectively, if Yb^{3+} and Er^{3+} form blended particles. According to literature,[22] Yb^{3+} has an absorption cross-section of 1.2×10^{-20} cm^2 sufficiently higher than 1.7×10^{-21} cm^2 for Er^{3+} ion at 980 nm. By taking Yb:Er molar ratio of 1:1 for the blended particle into consideration, the introduction of Yb^{3+} increases the particle absorbance by a factor of 4.0. To better compare with the $NaErF_4$ cores (15.6 nm), the

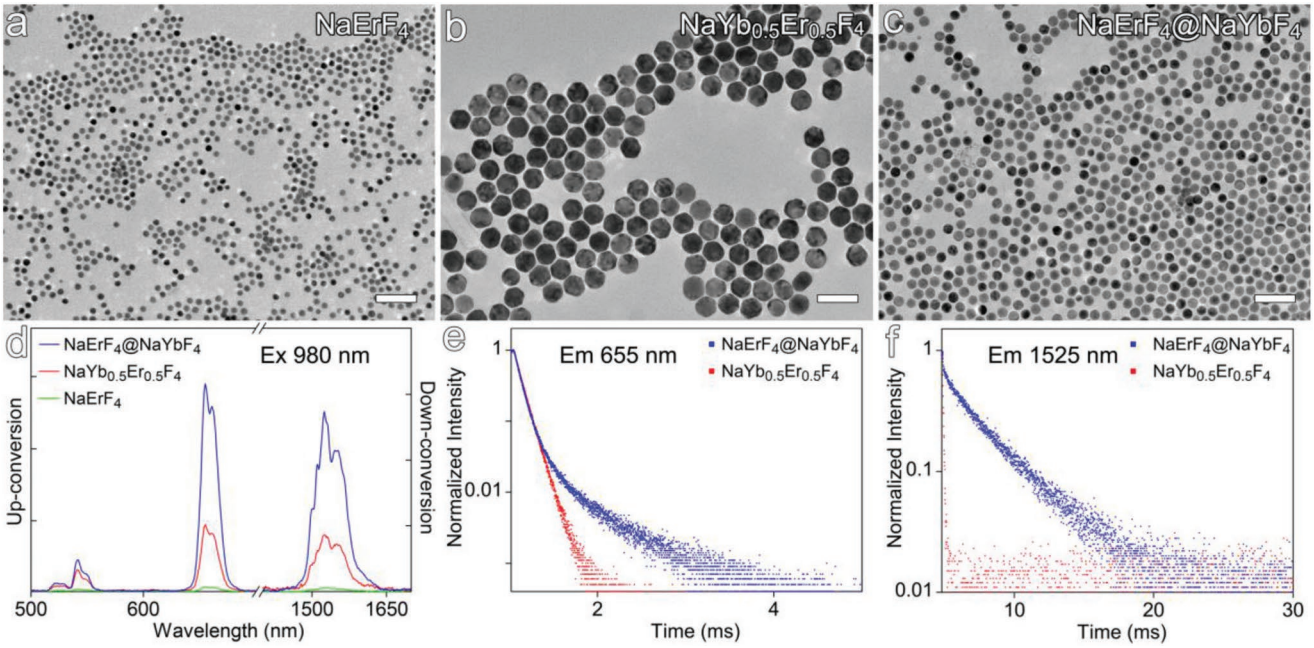

Figure 1. a–c) TEM images, normalized up- and down-conversion emission spectra recorded under excitation at d) 980 nm of $NaErF_4$, $NaYb_{0.5}Er_{0.5}F_4$, and $NaErF_4$@$NaYbF_4$, together with transient emissions observed at e) 655 and f) 1525 nm of $NaYb_{0.5}Er_{0.5}F_4$ and $NaErF_4$@$NaYbF_4$ nanocrystals. The embedded scale bars correspond to 100 nm.

synthetic conditions for $NaYb_{0.5}Er_{0.5}F_4$ particles were kept strictly identical. Nevertheless, the identical synthetic conditions led to 62 nm blended particles, which inevitably introduced an additional size effect favorable for the luminescence intensity. Thus, an enhancement factor contributed by the effects beyond the increased absorption of incident light can very roughly be estimated to be ≈3, based on aforementioned results. It was also quantitatively demonstrated that the luminescence can further be enhanced just by reconfiguring the particles from blended structure to core/shell structure. According to the results given in Figure 1d, both up- and down-conversion emissions are increased by factors of 36.0 and 38.0, respectively, if Yb^{3+} ions are placed in the shell around $NaErF_4$ cores. Since the introduction of Yb^{3+} can increase the absorbance by a factor of 4, the enhancement factor caused by the core/shell configuration can be roughly estimated to be one order of magnitude, suggesting that the introduction of shell is vital for suppressing the surface quenching effect, as previously observed.[23] In other words, if Yb^{3+} ions are placed in shells, both increased absorption and reduced surface quenching effect can simultaneously be achieved.

The photoluminescence of rare-earth nanoparticle is sensitive to its surface as the emitting ions sitting on the particle surface have different chemical environments involving capping agent, unsaturated coordination, and even dispersion medium, which form pathways for nonradiatively dissipating the adsorbed photoenergy into surroundings. To date, constructing core/shell structure to improve the photoluminescence intensity of core particles irrespective of the particle types is largely adopted, but the in-depth enhancing mechanisms can be different and remain to be elucidated. To understand the luminescence enhancement effect, time-resolved spectroscopy studies were carried out to compare transient optical properties of $NaErF_4$@$NaYbF_4$ and $NaYb_{0.5}Er_{0.5}F_4$ particles. As shown in Figure 1e,f, the transient decays of up- and down-conversion luminescence of $NaErF_4$@$NaYbF_4$ nanoparticles were fitted with detailed lifetimes being given in Table S1 in the Supporting Information. The average lifetime of up- and down-conversion emissions of $NaErF_4$@$NaYbF_4$ was of 103 µs and 2.9 ms, respectively, contrasting to 96 µs and 73.9 µs for $NaYb_{0.5}Er_{0.5}F_4$ nanoparticles, suggesting that the lifetime of up-conversion luminescence is only slightly prolonged in consequence of $NaYbF_4$ coating, while the lifetime of down-conversion emission is increased by a factor of 39.2. Because the measured lifetime is a combination of intrinsic lifetime which is constant for a certain energy level, and nonradiative transition lifetime which is directly related to surface quenching.[24] Hence, the substantially prolonged lifetime of 1525 nm emission suggests that $NaYbF_4$ shell can effectively block the nonradiative relaxation pathway for the down-conversion luminescence, which is apparently favorable for improving the intensity of the down-conversion luminescence. Nevertheless, $NaYbF_4$ is not an ideal material for forming a passivation shell as $^2F_{5/2}$ level of Yb^{3+} participates the direct energy transfer of the absorbed energy into surroundings under 980 nm excitation, which is supported by higher enhancement factors observed when $NaErF_4$@$NaYbF_4$ particles were excited under 808 nm, i.e., 46.4 and 97.0 for intensities of up- and down-conversion luminescence, respectively, as shown in Figure S2 (Supporting Information). The remarkably increased enhancement factors, especially for down-conversion luminescence at 1525 nm, strongly indicates that effectively reducing the energy transfer from Yb^{3+} to surroundings is important for further improving the up- and down-conversion luminescence. Therefore, the $NaErF_4$@$NaYbF_4$ particles were further coated with $NaYF_4$ shell as Y^{3+} has no suitable energetic levels participating the energy transfer to surroundings.

In addition, to show the $NaYbF_4$ thickness-dependent sensitization effect, the $NaYbF_4$ layer thickness was also varied.

2.2. Synthesis and Optical Properties of $NaErF_4$@$NaYbF_4$@$NaYF_4$ Nanocrystals with Different $NaYbF_4$ Layer Thicknesses

In detail, three samples were prepared. In the first one as shown in **Figure 2**a, the initial $NaErF_4$ core is of 21.0 ± 0.8 nm, while the successive growth of $NaYbF_4$ and $NaYF_4$ shells further increases the particle size up to 23.0 ± 0.9 and 31.7 ± 1.5 nm, respectively. Therefore, the $NaYbF_4$ thickness in the first sample is about 1.0 nm. In the second sample as shown in Figure 2b, the size of $NaErF_4$ core, $NaErF_4$@$NaYbF_4$, and $NaErF_4$@$NaYbF_4$@$NaYF_4$ nanoparticles is of 20.0 ± 0.7, 24.0 ± 1.1, and 30.1 ± 1.3 nm, respectively, which gives rise to a $NaYbF_4$ thickness of 2.0 nm. The third sample was prepared by over-coating the $NaErF_4$@$NaYbF_4$ particles shown in Figure 1c with $NaYF_4$. The size of $NaErF_4$ core (Figure 1a), $NaErF_4$@$NaYbF_4$ (Figure 1c), and $NaErF_4$@$NaYbF_4$@$NaYF_4$

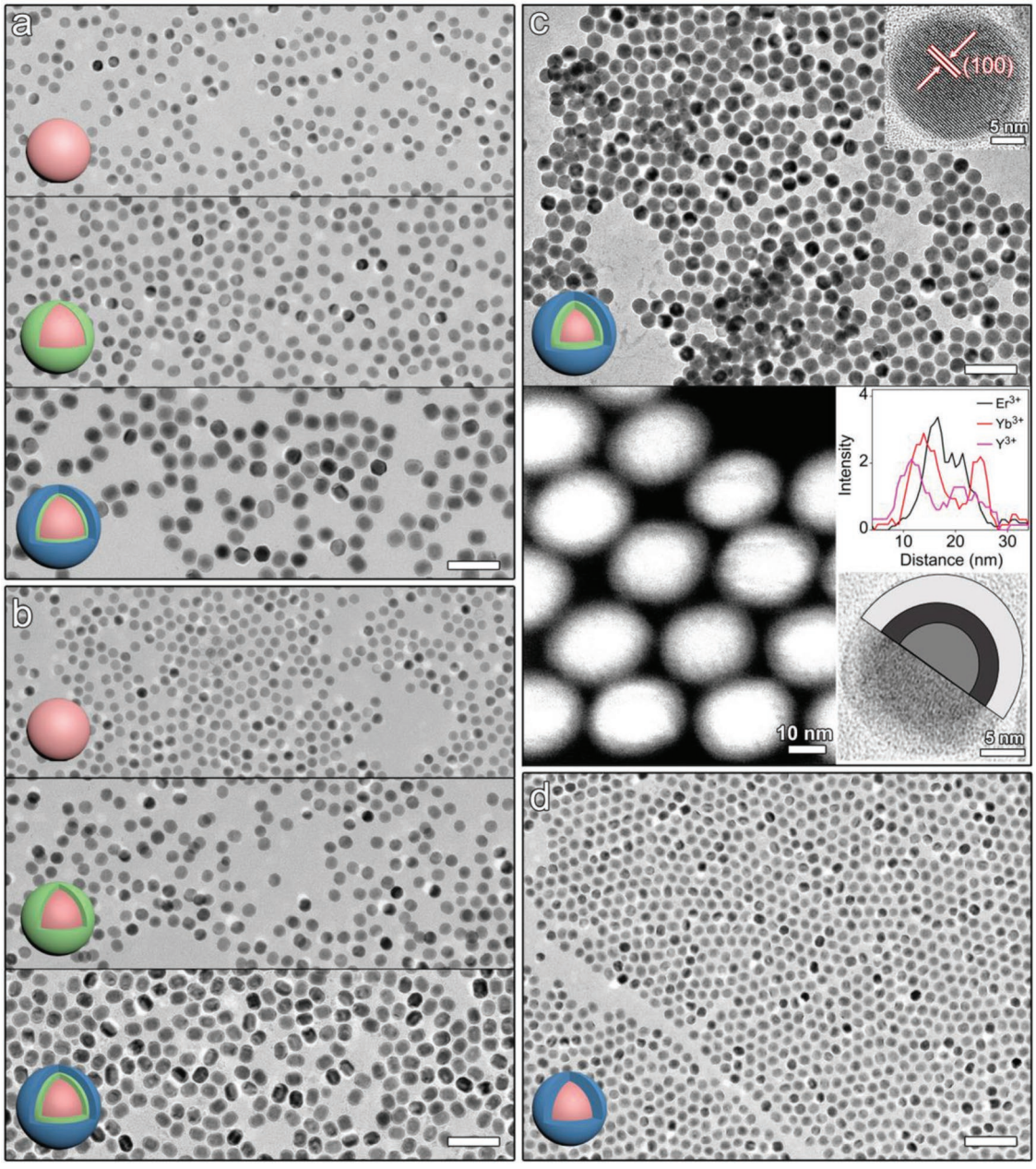

Figure 2. TEM images of $NaErF_4$, $NaErF_4$@$NaYbF_4$, and $NaErF_4$@$NaYbF_4$@$NaYF_4$ nanocrystals with the thickness of $NaYbF_4$ layer tuned from a) 1.0, b) 2.0, to c) 3.7 nm, together with insets in frame c including HRTEM image of a single IST3.7 particle (top panel), HAADF-STEM image of IST3.7 particles (left of bottom panel), line spectra of the lanthanide elements across a selected particle detected through energy dispersive spectroscopy (right-top of bottom panel), high magnification TEM image of a single IST3.7 particle (right-bottom of bottom panel), and d) IST0 which possesses no intermediate $NaYbF_4$ layer. The scale bars embedded in frame (a)–(d) correspond to 100 nm.

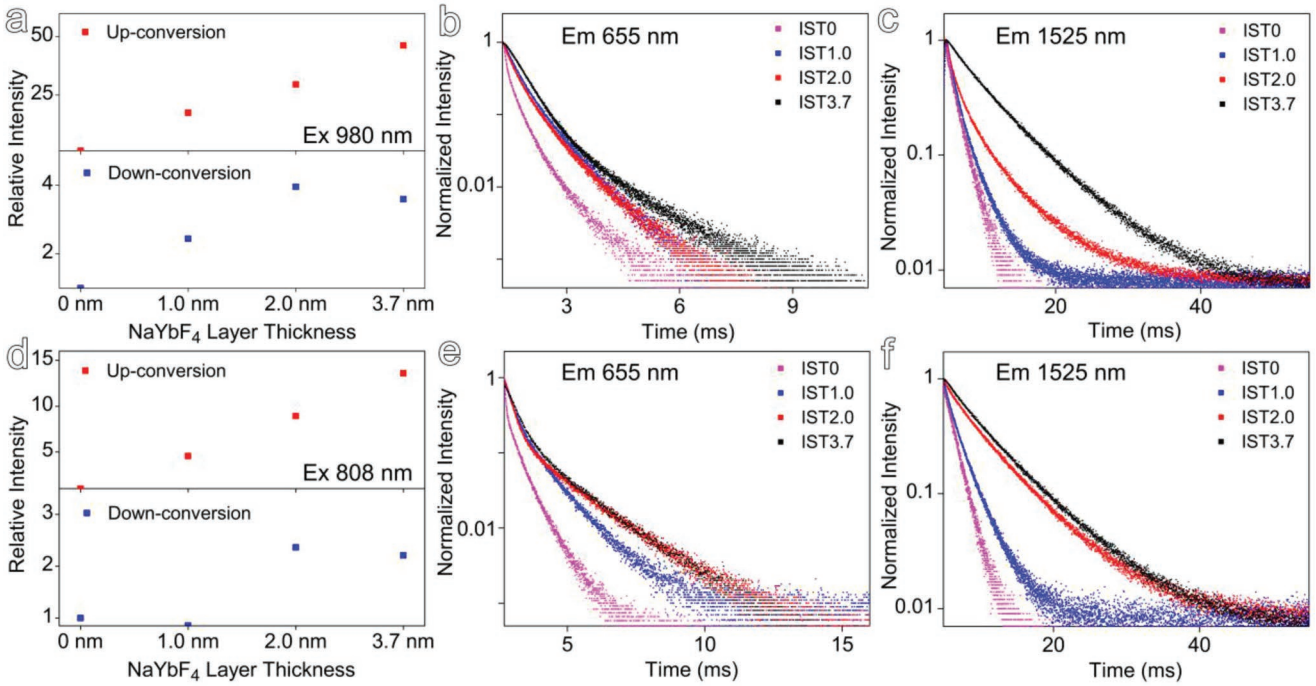

Figure 3. The static and transient emissions of up- and down-conversion luminescence of $NaErF_4$@$NaYbF_4$@$NaYF_4$ nanoparticles with tuned $NaYbF_4$ layer thicknesses recorded under a–c) 980 and d–f) 808 nm excitation, respectively.

(the top panel of Figure 2c) core/shell nanoparticles is of 15.6 ± 0.7, 23.0 ± 1.7, and 30.6 ± 1.7 nm, respectively, i.e., the thickness of $NaYbF_4$ shell in the third sample is of 3.7 nm. According to $NaYbF_4$ intermediate shell thickness (IST), the above $NaErF_4$@$NaYbF_4$@$NaYF_4$ particle samples were named as IST1.0, IST2.0, and IST3.7, respectively, in the following discussion.

To confirm the formation of the core/shell/shell structure, IST3.7 was characterized with high-resolution TEM (HRTEM) and high-angle annular dark field scanning transmission electron microscopy (HAADF-STEM). As shown in the inset of the top panel of Figure 2c, the core/shell/shell particles exhibit clear lattice fringes with a measured d-spacing of 0.50 nm which is well consistent with the lattice spacing in the (100) planes of hexagonal-phased $NaYF_4$. As HAADF-STEM is more sensitive to atomic number, it was further used to show the core/shell structures of the particles. The HAADF-STEM image in the left frame of the bottom panel of Figure 2c shows a clear radial contrast caused by the radial distribution of different lanthanide elements in the particles, which is better reflected in the energy dispersive spectra recorded across the center of a selected particle (right-top frame of the bottom panel of Figure 2c). In fact, the $NaLnF_4$ particles are very sensitive to electron beam radiation.[25] However, particles showing core/shell structures can occasionally be observed under a high magnification as shown in right-bottom frame of the bottom panel of Figure 2c.

The above experimental results indicate that the core/shell/shell particles can be prepared with the thickness of the intermediate $NaYbF_4$ shell being precisely tuned. For better understanding the effects of $NaYbF_4$ layer on optical properties of the core/shell/shell particles, $NaErF_4$@$NaYF_4$ particles of 22.5 ± 1.1 nm with average core size of 15.6 ± 0.7 nm were prepared, as shown in Figure 2d, and denoted as IST0 since no $NaYbF_4$ intermediate shell was present in this sample. The integrated up- and down-conversion emission intensities of $NaErF_4$@$NaYbF_4$@$NaYF_4$ particles acquired upon 980 nm excitation against the $NaYbF_4$ IST are shown in **Figure 3**a. In comparison with IST0, IST1.0 particles present up- and down-conversion emissions with intensity being enhanced by factors of 17.3 and 2.4, respectively, which well manifests the role of $NaYbF_4$ layer as it can better absorb 980 nm laser excitation than the core particles. It is also shown that with the increase of $NaYbF_4$ layer thickness from 1.0 to 3.7 nm, the up- and down-conversion emissions are further enhanced by 2.7 and 1.5 times, respectively. Although the up-conversion emission intensity monotonically increases against $NaYbF_4$ layer thickness, the down-conversion emission presents a nonmonotonic behavior with the maximum emission showing at 2.0 nm for IST. This can be understood through the difference between the transitions involved in up- and down-conversion luminescence, which are shown in Figure S3 (Supporting Information). The up-conversion emission requires multiphoton absorption. Therefore, the probability of excited state absorption will be increased against IST, which is favorable for up-conversion luminescence. In addition, there are multiple energy transfer pathways involved in up-conversion emission. Taking 655 nm emission as an example, Yb^{3+} ions donate their energy to Er^{3+} ions by promoting the Er^{3+} ions to their excited state ($^4I_{11/2}$). Subsequently, two different pathways will be taken by Er^{3+} ions to return to the ground states to emit 655 nm photon. In the first pathway, Er^{3+} ions are populated to higher excited states ($^4F_{7/2}$) via resonant energy transfer from Yb^{3+} ions. The super-excited Er^{3+} ions ($^4F_{7/2}$) are then nonradiatively relaxed to the $^4F_{9/2}$ state, followed by subsequent radiative transition to $^4I_{15/2}$,

which gives rise to 655 nm emission. In the second pathway, the excited Er^{3+} ions ($^4I_{11/2}$) are first relaxed to $^4I_{13/2}$, then the excited electrons are populated to a higher excited state ($^4F_{9/2}$) again by resonate energy transfer from Yb^{3+} ions. From there, the radiative transition process occurs similar to that in the first pathway. Different from the up-conversion process, the down-conversion emission of Er^{3+} ions requires single photon absorption. Then, the excited Er^{3+} ions ($^4I_{11/2}$) are nonradiatively relaxed to the $^4I_{13/2}$, followed by a radiative transition to ground state ($^4I_{15/2}$) to emit 1525 nm light. As the population of $^4I_{13/2}$ level is easily saturated, a maximum $NaYbF_4$ layer thickness is easily reached as seen in Figure 3a, which leads to an absolute fluorescence QY up to 18.7% at room temperature for the NIR II emission at 1525 nm. The QY was measured with an integrating sphere under 980 nm excitation (10 W cm^{-2}). In fact, the absolute fluorescence QY of 1525 nm emission up to 32.8% was previously reported for 200 nm $NaCeF_4$:Er/Yb nanoparticles.[26] However, the QY of lanthanide nanoparticles is strongly particle-size dependent,[27] which can also be seen from the results given in Figure 1d. The current QY is in fact very remarkable for particles smaller than 50 nm as they are more suitable for in vivo applications than the large counterparts.[28] Different from the down-conversion luminescence, the up-conversion luminescence involves multiple levels for hosting excited electrons, the population of different levels associated with up-conversion luminescence are far from saturated under the current experimental conditions. Therefore, the up-conversion luminescence keeps increasing in intensity against the $NaYbF_4$ layer thickness, which also suggests there remains a big room to further increase the up-conversion luminescence intensity of the current particles, although the up-conversion emission of IST3.7 is increased by a factor of 46, if compared with that of IST0 shown in Figure 2d.

The transient emissions at 655 and 1525 nm were also recorded to show the impact of $NaYbF_4$ layer thickness. The results given in Figure 3b,c and Table S2 (Supporting Information) clearly revealed that the lifetime of these two emissions is dependent on the $NaYbF_4$ layer thickness. For example, with the increase of IST, the lifetime of 655 nm emission is generally increased, e.g., from 317 µs for IST0 to 549 µs for IST3.7. If further comparing IST3.7 with $NaErF_4$@$NaYbF_4$, the lifetime is increased by a factor of >5. The lifetime of 1525 nm emission is however monotonically prolonged against the IST, e.g., from 1.5 ms for IST0 to 5.9 ms for IST3.7. If comparing IST3.7 with $NaErF_4$@$NaYbF_4$ cores, the lifetime is prolonged by a factor of ≈2.0. All these data suggest that the lifetime of down-conversion emission is more sensitive to the IST, probably because the nonradiative channel is dominated by energy transfer directly from the core into surroundings including surface ligand and solvent. In contrast, the lifetime of up-conversion emission is dependent not only on the IST but also on energetic levels of the shell. In other words, the nonradiative relaxation may occur through cross-relaxation involving energy levels in the shell, such as $^2F_{5/2}$ of Yb^{3+} ions. Hence, $NaYF_4$ coating is more favorable for improving the intensity of up-conversion luminescence (Figure 3a). For example, the intensity of 655 nm emission is increased by 440 times if $NaErF_4$@$NaYbF_4$ (Figure 1c) was coated with $NaYF_4$ (Figure 2c). Similar transient behaviors were also observed when the corresponding particles were subjected to 808 nm excitation, as shown in Figure 3e,f and Table S2 (Supporting Information). Nevertheless, the static luminescence intensities of both up- and down-conversion luminescence were lower than those recorded under 980 nm excitation, as shown in Figure 3d, because Yb^{3+} is more favorable for being excited at 980 nm rather than 808 nm.

2.3. Preparation of the Tumor Imaging Probe

Based on above investigations, IST3.7 with well-balanced up- and down-conversion luminescence was chosen for the following tumor imaging studies. Although in vivo imaging through up- and down-conversion luminescence of lanthanide nanoparticles have been widely reported,[29] to combine the up- and down-conversion emissions of the same particle is apparently advantageous. It has been demonstrated that the up-conversion luminescence can be used to visualize tumors smaller than 2 mm and lymphatic micro-metastasis smaller than 1 mm in vivo, owing to the high quantum efficiency of sensors for visible lights.[15,20a] Moreover, the up-conversion luminescence of lanthanide nanoparticles holds great potentials for surgical navigation as long as the luminescence intensity is high enough. While the NIR II emission presents great advantages in visualizing the targeting area with greatly improved resolution and signal-to-noise ratio, although the detection of NIR II emission remains very costly. To this end, IST3.7 was first PEGylated through ligand exchange following a protocol reported before.[30] In detail, an asymmetric polyethylene glycol (PEG) bearing a maleimide group at one end and a diphosphate group at the other (mal-PEG-dp) was used to replace the oleic acid (OA) ligands to render the core/shell particles water-soluble. The resulting PEGylated nanoparticles, as displayed in Figure S4a (Supporting Information), presented excellent colloidal stability in both water and phosphate buffer saline (PBS) buffer,[20a,31] which is favorable for a long blood residence time. To improve the tumor targeting ability, FA whose receptor overexpressed in cancers such as colorectal cancer, ovarian cancer etc., was chosen to construct the tumor-specific nanoprobe. Upon covalent conjugation, FA was coupled onto the surface of the PEGylation nanoparticles, and resulting nanoparticle/folic acid conjugate was named as NP-FA, as shown in Figure S4b (Supporting Information). The absorption spectroscopy and dynamic light scattering (DLS) results shown in **Figure 4**a,b demonstrate that NP-FA nanoprobe is successfully constructed and no particle agglomeration occurred during the conjugation reaction. In addition, the optical properties including up- and down-conversion luminescence remain nearly unchanged throughout the conjugation reaction, as shown in Figure 4c.

2.4. Cytotoxicity and Targeting Ability of the NP-FA Probes In Vitro

Before validating the targeting ability, the cytotoxicity of the NP-FA probe was investigated through methyl thiazolyl tetrazolium

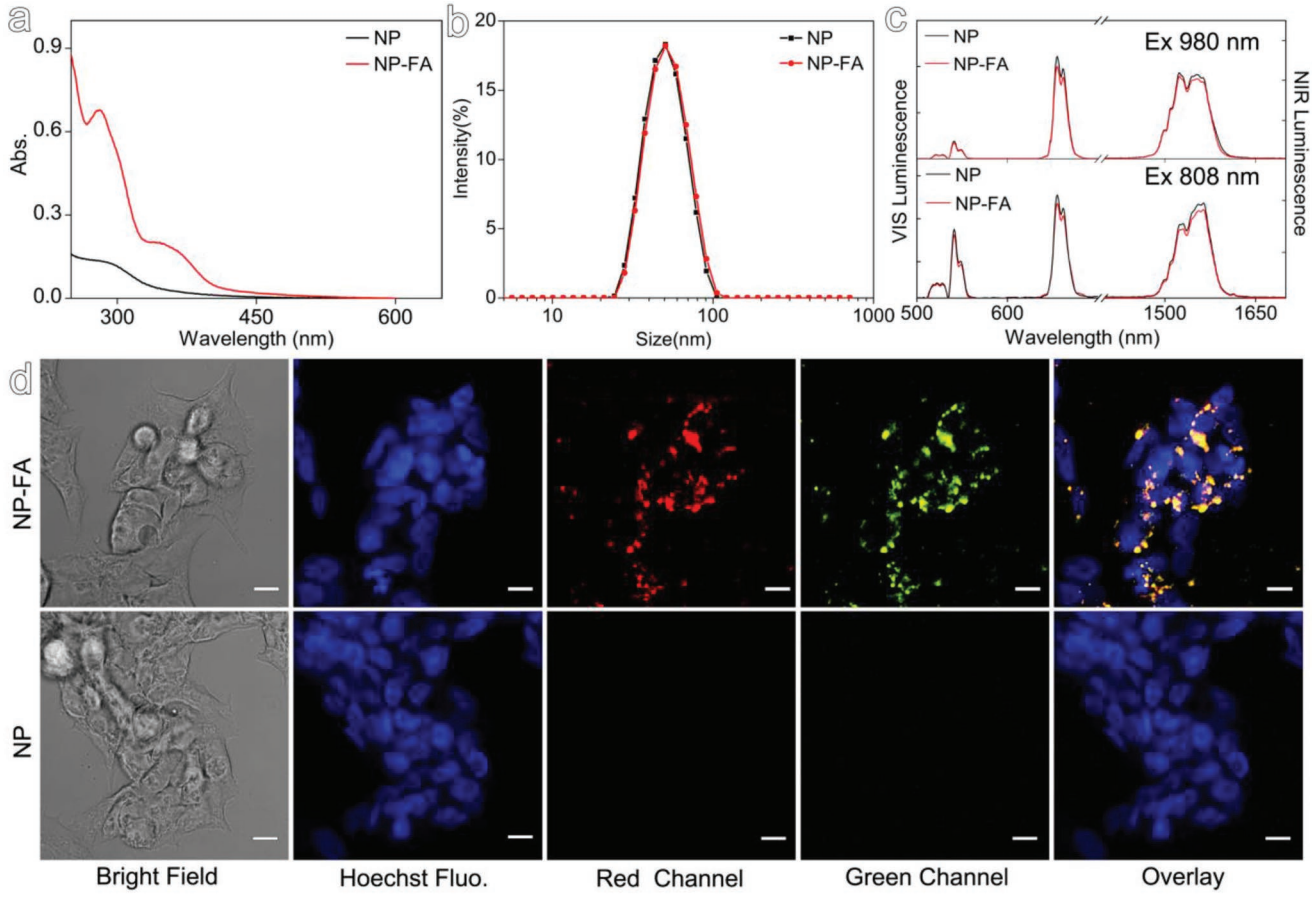

Figure 4. Top panel: a) absorption spectra, b) hydrodynamic size distribution profiles, and c) up-/down-conversion luminescence recorded under 980 and 808 nm laser excitations, respectively of NP and NP-FA conjugates. d) Bottom panel: bright field images, fluorescence images (Hoechst Fluo.) collected through 420–520 nm window for imaging the nuclei stained with Hoechst, up-conversion luminescence images collected through 604–696 nm (Red Channel) and 506–594 nm (Green Channel), respectively, together with merged images (Overlay) of LS180 cells incubated with NP-FA and NP, respectively (the scale bars correspond to 10 μm; the experimental conditions for in vitro cell studies were optimized so as to maximally show the difference in cellular uptake between NP-FA and NP).

(MTT) assays on the proliferation of LS180 cells. As shown in Figure S5 (Supporting Information), both NP-FA and its mother particle did not show significant cytotoxicity when Er^{3+} concentration was below 20 mmol L^{-1} that is two orders of magnitude higher than the dose for in vivo imaging. Then, the targeting ability of the NP-FA probes in recognizing LS180 cells whose surface expresses folate receptor (FR) was demonstrated through in vitro cell binding assays. As displayed in Figure 4d, the cells coincubated with the NP-FA probes show intense up-conversion emission signals through two bandpass filters of 506–594 nm (Green Channel) and 604–696 nm (Red Channel), respectively, under 980 nm laser excitation. Further merging the upconversion luminescence image with the fluorescence image of the cells stained with Hoechst for nuclei reveals that the nanoprobes are mainly populated in cytoplasm, probably through receptor-mediated endocytosis. In contrast, no up-conversion signal was detected from the cells incubated with the PEGylation nanoparticles that bear no surface folic acid ligand. These results positively demonstrated the NP-FA nanoprobe has a remarkable binding specificity toward its target, i.e., tumor cells expressing FR.

2.5. Up- and Down-Conversion NIR II Imaging of Subcutaneous and Intraperitoneal Tumor Xenografts In Vivo

Long blood residence time is preferred for effectively targeting tumors with any given imaging probes. For the current studies, the blood half-times of NP-FA and its control nanoparticles were determined with single-photon emission computed tomography. By fitting the blood residence time, the blood half-time was calculated to be 158 and 164 min for NP-FA and the mother PEGylated nanoparticles, respectively (Figure S6, Supporting Information). To investigate the tumor imaging capacity of the NP-FA probe in vivo, two types of mouse tumor models were established upon subcutaneous or intraperitoneal injection of LS180 cells into 4-week-old BALB/c nude mice. After intravenously delivering the NP-FA probe, the tumor-bearing mice were imaged with the aid of different types of filters. The optical images were captured through up- and down-conversion luminescence, respectively, at different time points postinjection of the NP-FA probe. Regarding the subcutaneous tumor, the results shown in **Figure 5**a reveal that the luminescence signal at tumor site appears 1 h postinjection of the probe and

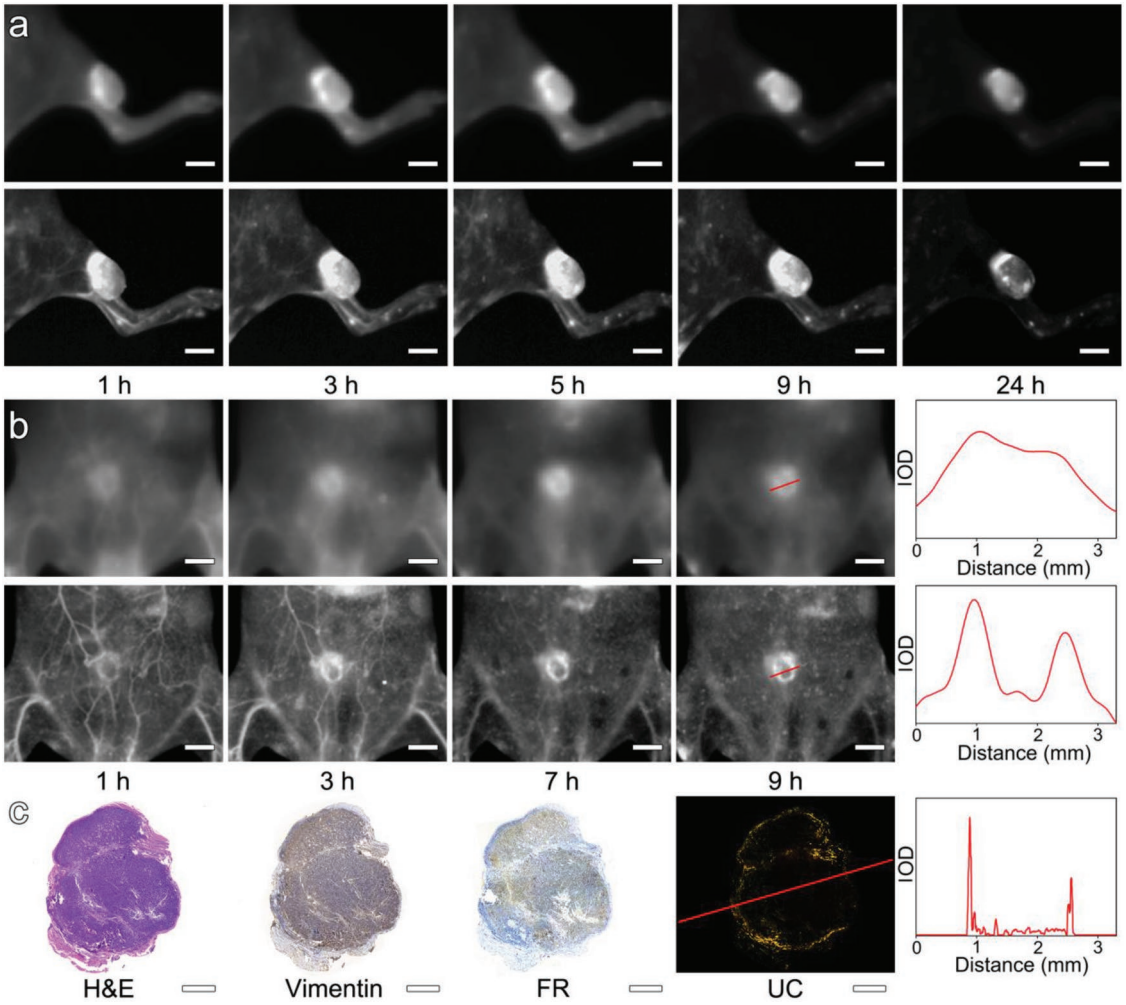

Figure 5. Up-conversion (top) and down-conversion (bottom) luminescence images of a) subcutaneous and b) intraperitoneal tumors in vivo recorded at different time points postinjection of NP-FA, together with c) microscopic images of adjacent slices of intraperitoneal tumor extracted upon H&E staining or immunohistochemical staining through antivimentin antibody and anti-FR, respectively. The up- and down-conversion luminescence images of the same tumor were recorded under 980 nm excitation and 808 nm excitation, respectively. The resolution of up-/down-conversion luminescence imaging can be compared through the line spectra drown across the tumorous regions in vivo. The scale bars (a,b) correspond to 3 mm. The scale bars in (c) correspond to 500 µm.

reaches a maximum at 5 h postinjection. The signal intensity remains at its maximum for nearly 4 h and then gradually decays over a day. As shown in Figure S7 (Supporting Information), the signal evolutions for both up- and down-conversion luminescence are nearly identical, suggesting that both of these two emissions are fairly stable under physiological conditions at least over the inspection time window of 24 h. Nevertheless, the 1525 nm emission gives rise to much sharper images contrasting to 655 nm emission that generates to blurry ones. This difference persists even after the tumors and organs were extracted 24 h postinjection, as shown in Figure S8 (Supporting Information). Apparently, imaging through 1525 nm emission can better present the detailed structure of the region of interest (ROI) owing to the greatly suppressed background noise, particularly the tissue autofluorescence that is strongly wavelength-dependent as shown in Figure S9 (Supporting Information), i.e., the longer the emission wavelength is, the lower the background noise will be. It should be mentioned that the mother nanoparticle gave rise to very low tumor uptake at the same dose level with respect to Er^{3+} as shown in Figure S10 (Supporting Information). The limited tumor uptake (≈2.2% ID g^{-1}) was probably caused by the well-known enhanced permeability and retention effect, while the tumor uptake of the NP-FA particle probe reached 5.2% ID g^{-1}, determined by ICP-AES, as shown in Figure S11 (Supporting Information). Therefore, it can be concluded that the NP-FA nanoprobe possesses remarkable tumor targeting specificity and the NIR II emission is superior for precisely showing the detailed structures of ROI, which encouraged us to image the intraperitoneal tumors that are embedded in an environment more complicated than that for subcutaneous tumors.

The results shown in Figure 5b reveal that the intraperitoneal tumor starts to show the optical signal 1 h postinjection. Then, the signal of tumor site reaches its maximum ≈3 h postinjection and maintains nearly unchanged over the following 6 h. This signal evolution tendency is rather in consistence with

that from the subcutaneous tumors. Apart from that, the down-conversion luminescence imaging shows much higher spatial resolution than the up-conversion luminescence imaging, which can be clearly seen from the line-scanning spectra drawn across the tumorous region. In consequence, the blood vessel systems are clearly presented. Owing to the improved spatial resolution, an unambiguous boundary of the tumor site is also displayed, suggesting an uneven distribution of FR that are strongly associated with proliferation, invasion, and metastasis of cancers.[32]

2.6. Histochemical and Immunohistochemical Studies of Intraperitoneal Tumor

To confirm the higher expression of FR at tumor boundary, the intraperitoneal tumor was extracted postimaging, sliced, and then stained for the histochemical and immunohistochemical (IHC) analysis. As shown in Figure 5c, hematoxylin and eosin (H&E) staining results in an obvious demarcation line between the tumor and the muscle tissues. Close to this boundary line, vimentin as a biomarker for epithelial-mesenchymal transition (EMT) is up-regulated according to the IHC analysis, indicating a strong local invasion and metastasis tendency of this tumor. Moreover, a rather similar distribution pattern is also observed for FR that is a stimulus for tumor cell proliferation and metastasis. Via the up-conversion luminescence collected through red (604–696 nm) and green (506–594 nm) channels, an adjacent tumor slice was imaged through confocal microscopy. Owing to the extraordinarily high QY, the distribution of NP-FA nanoprobes across the entire tumorous region, particularly the tumor boundary can clearly be seen as indicated by the spectrum along the line randomly drawn across the tumorous region. Although the boundary indicated by the optical signal is sharper than those derived from FR and vimentin staining, they are generally in consistent. Moreover, the ex vivo imaging obtained through the NP-FA probe perfectly matches the in vivo imaging results shown above, suggesting that the sharp boundary of the tumors reflected by NIR II emission may collectively be contributed by the locally up-regulated expression of FR, rich blood vessels, and poor perfusion of the tumor as well. Nevertheless, both in vivo and ex vivo imaging results also suggest that the current nanoprobe may potentially be used for noninvasively showing biodistribution of specific targets owing to its remarkable QY and suitable NIR II emission for high resolution imaging.

In addition, the potential side effect of the NP-FA probes was also investigated through histological analysis of the major organs of a group of mice ($n = 3$) extracted 30 d postinjection of NP-FA. As displayed in Figure S12 (Supporting Information), no noticeable inflammation or damage was observed in heart, kidney, liver, lung, and spleen, which highlights the safety feature of the NP-FA probe.

3. Conclusion

In summary, by spatially separating the emitting Er^{3+} ions from the sensitization Yb^{3+} ions, nanoparticles composed of high Er^{3+} concentration core and Yb^{3+} shell were prepared to obtain highly luminescent NIR II nanoparticles. The detailed static and transient spectroscopy studies revealed that the surface coating of $NaYbF_4$ over $NaErF_4$ cores can simultaneously enhance the up- and down-conversion luminescence of the latter. However, owing to the involvement of the energetic levels of Yb^{3+} in nonradiative relaxation, $NaYF_4$ shell was further introduced to improve the up- and down-conversion luminescence of the $NaErF_4$ cores. By tuning the thickness of the intermediate $NaYbF_4$ layer, it was demonstrated that the nonradiative relaxation for down-conversion luminescence is more shell thickness-dependent, while that for up-conversion luminescence is sensitive to the presence of specific energy levels in the shell. Based on the above understanding, the structural parameters of $NaErF_4@NaYbF_4@NaYF_4$ nanoparticles were optimized and absolute fluorescence QY up to 18.7% was obtained for 1525 nm emission of particles of ≈30 nm at room temperature. The perfect combination of the outstanding up- and down-conversion luminescence performance was thus enabled as they are advantageous in different imaging applications. The $NaErF_4@NaYbF_4@NaYF_4$ nanoparticles were PEGylated and then covalently conjugated with FA. The resulting particle probe presented excellent safety profile and outstanding tumor cell binding specificity in vitro. The images of subcutaneous tumors recorded through up- and down-conversion emissions, respectively, presented the advantages of NIR II emission in achieving high spatial resolution and high signal-to-noise ratio images, which allowed to image the intraperitoneal tumors with heterogeneous expression of FR. The high expression of FR at tumor boundary was further confirmed through careful immunohistochemical analysis and confocal up-conversion luminescence imaging of the tumor ex vivo. In conclusion, we propose an innovative particle structure in which the emitting Er^{3+} ions and sensitization Yb^{3+} ions are spatially separated to maximize the emissions of Er^{3+} and thus provide a platform not only useful for sensitive tumor diagnosis through different optical windows of tissues, but also potentially suitable for showing the heterogeneous expression of pathological indicators in vivo.

4. Experimental Section

Reagents and Materials: OA(364525), 1-octadecene (ODE, O806), ammonium fluoride (NH_4F, 216011), $Er(CH_3COO)_3 \cdot xH_2O$ (325570), $Yb(CH_3COO)_3 \cdot xH_2O$ (544973), $Y(CH_3COO)_3 \cdot xH_2O$ (326046), FA (F7876), MTT (M2128), pentobarbital sodium (P3761), and PBS (P5493) were purchased from Sigma-Aldrich. Mal-PEG-dp and Jeffamine-modified FA were customized products provided by Beijing Oneder Hightech Co. Ltd. Human colorectal cancer cell line LS180 was obtained from the Oncology School of Peking University. Dulbecco's modified Eagle medium (DMEM) high glucose (HyClone), F-12K Nutrient Mixture (Gibco), fetal bovine serum (HyClone), penicillin, and streptomycin were bought from Beijing Biodee Biotechnology Co. Ltd. Other analytical grade chemicals, such as sodium hydroxide, ethanol, cyclohexane, dimethyl sulfoxide (DMSO), and tetrahydrofuran (THF) were bought from Sinopharm Chemical Reagent Beijing, Co., Ltd and used as received.

Synthesis of $NaErF_4$ Core Nanocrystals: The $NaErF_4$ core particles were prepared according to a literature method. In a typical preparation, 0.8 mmol $Er(CH_3COO)_3 \cdot xH_2O$ was added into a mixture of OA (6 mL) and ODE (14 mL) in 100 mL flask at the room temperature. The mixture was heated to 150 °C under vacuum and then kept at this temperature

for ≈30 min to obtain a homogeneous solution. A methanol solution of 10 mL containing NaOH (2.0 mmol) and NH_4F (3.2 mmol) were added dropwise after the solution was cooled down to 50 °C. The reaction system was stirred for another 30 min at this temperature. Then, the reaction temperature was raised to 100 °C to remove the methanol under the vacuum and then maintained for 10 min. Subsequently, the reaction temperature was improved to 290 °C with temperature-increasing rate of 20 °C min^{-1}. After reaction at this temperature for another 2 h. Finally, the reaction system was cooled to room temperature. The nanoparticles were precipitated by ethanol and collected by centrifugation for several cycles and then redispersed in cyclohexane for further use. The $NaYb_{0.5}Er_{0.5}F_4$ nanoparticles were prepared exactly by the above mentioned process except that 0.4 mmol $Er(CH_3COO)_3 \cdot xH_2O$ and 0.4 mmol $Yb(CH_3COO)_3 \cdot xH_2O$ were simultaneously introduced into the mixture of OA (6 mL) and ODE (14 mL) to obtained the stock solution for the following reaction.

Synthesis of $NaErF_4$@$NaYbF_4$ Core/Shell Nanocrystals: Core/shell nanocrystals were prepared through an epitaxial growth approach by using the as-prepared of $NaErF_4$ particles as cores. Typically, $Yb(CH_3COO)_3 \cdot xH_2O$ (0.4 mmol) was added into a 50 mL flask containing 7 mL of ODE and 3 mL of OA. The mixture was kept at 150 °C for 30 min to form Yb-oleate complexes. After the temperature of Yb-oleate precursor solution was cooled down to room temperature, 0.4 mmol of $NaErF_4$ nanoparticles dispersed in 4 mL of cyclohexane were introduced, and the resulting mixture was then heated at 80 °C to remove the cyclohexane under vacuum. Subsequently, the reaction solution was cooled to 50 °C. A methanol solution of 6 mL containing 1.0 mmol of NaOH and 1.6 mmol of NH_4F was introduced dropwise. Then the reaction mixture was processed according to the same procedures according to those described for preparing the core particles. The tunability of the $NaYbF_4$ intermediate layer thickness was realized by varying the amount of Yb shell precursor and the amount of NaOH and NH_4F for growing $NaYbF_4$ accordingly, with the rests remaining unchanged. The above procedures were also used to prepare $NaErF_4$@$NaYF_4$ core/shell nanocrystals.

Synthesis of $NaErF_4$@$NaYbF_4$@$NaYF_4$ Core/Shell/Shell Nanocrystals: Core/shell/shell nanocrystals were prepared through further epitaxial growth of $NaYF_4$ according to the procedures mentioned above for growing $NaYbF_4$ intermediate layer.

Preparation of Water-Soluble Nanoparticles: The water-soluble nanoparticles were prepared via a ligand exchange reaction. ≈5 mL THF containing 10 mg of purified nanoparticles was dropwise added into 5 mL of THF containing 100 mg of mal-PEG-dp. After the ligand exchange reaction took place overnight at room temperature, the PEGylated particles were precipitated by cyclohexane and then washed with cyclohexane for three cycles, dried under vacuum at room temperature and finally dispersed in Milli-Q water for further use.

Characterization of the Nanoparticles: The TEM and HRTEM were carried out with Hitachi HT-7700 and JEM 2100F microscopes operating at 120 and 200 kV, respectively, for characterizing the particle size, shape, crystalline structure. The particle size was determined by counting more than 300 particles per sample. In addition, the SAED measurements were carried out for further showing the phase structure of the resulting nanocrystals. The concentration of the rare earth elements in different samples was determined by using ICP-AES 6300DV after the particles were eroded with a concentrated mixture of nitric acid and hydrogen peroxide. The up- and down-conversion luminescence spectra were measured by Edinburgh Instruments FLS 920 equipped with 980 and 808 nm CW laser diodes (1 W) as the excitation sources. The transient up- and down-conversion luminescence was recorded on Deltaflex Fluorescence Lifetime Instrument (HORIBA) amounted with 980 and 808 nm pulsed laser diodes. The absolute QY was measured with an integrating sphere (Edinburgh) under 980 nm laser excitation and the luminescence was detected with a NIRPMT (R5509) detector. DLS measurements were carried out at 298.0 K with Nano ZS (Malvern) equipped with a solid state He-Ne laser (λ = 632.8 nm) for monitoring the hydrodynamic profiles of the particles.

Preparation of the Nanoprobes: Jeffamine modified FA was covalently conjugated to the PEGylated $NaErF_4$@$NaYbF_4$@$NaYF_4$ nanoparticles via "click" reaction. In detail, ≈0.5 mg of jeffamine-modified FA was mixed with 0.2 mg of 2-iminothiolane hydrochloride in 1 mL water, and the reaction mixture was kept at room temperature for 2 h. Then, 6 mg of PEGylated nanoparticles was added into the above solution and the conjugation reaction was allowed for 30 min. The resulting NP-FA conjugates were purified with 30 k MWCO centrifugal devices to remove the unreacted jeffamine-FA, then transferred into 1 × PBS buffer, and finally stored at 4 °C for further use.

Cell Culture and In Vitro Cellular Imaging: Human colorectal cancer cell line LS180 was cultured in a medium of DMEM high glucose and F-12K nutrient mixture (1:1) supplemented with 10% fetal bovine serum and 1% penicillin-streptomycin solution (100 ×) at 37 °C under a 5% CO_2 atmosphere. MTT assays were carried out to study the cytotoxicity. Typically, LS180 cells were seeded into a 96-well cell culture plate by 5×10^3 cells per well under 100% humidity, and then cultured at 37 °C in an atmosphere containing 5% CO_2 for 24 h. The NP-FA and the mother PEGylated particle were added into the wells by a series of concentrations, respectively, and incubated with the cells for 24 h at 37 °C under 5% CO_2. Subsequently, the supernatant containing the excrescent samples was decanted, and the cells were incubated for another 48 h at 37 °C under 5% CO_2. After that, 10 µL of MTT (5 mg mL^{-1}) was added to each well and incubated for 4 h at 37 °C under 5% CO_2. Thereafter, 150 µL of DMSO was added into every well, and the assay plate was shaken at 37 °C for 15 min. The optical density of each well at 490 nm was recorded on a microplate reader (Thermo, Varioskan Flash), while the optical density at 630 nm was used as reference.

The in vitro cellular imaging was then carried out for verifying the binding specificity of the nanoprobes to their targets. Approximately, 10^6 LS180 cells were seeded in the wells of two confocal capsules and incubated overnight at 37 °C under 5% CO_2 to allow a firm adherence. After being rinsed with PBS buffer, the cells were incubated with the nanoprobes and the nanoparticles, respectively, for 6 h at 37 °C. After that, the cells were rinsed three times with PBS to remove the unbound particles. The cells were further incubated with 5 µg mL^{-1} Hoechst 33 342 for nuclei staining. The cell images were observed with a confocal microscope (A1R-Nikon) equipped with 980 nm CW laser. The luminescence signals through Green Channel (506–594 nm) and Red Channel (604–696 nm) were collected. For the nuclei imaging, the excitation line was tuned to 405 nm and the fluorescence signals were collected in through a transparent range of 420–520 nm.

Pharmacokinetics of NP-FA Nanoprobes: The NP-FA and nanoparticles were labeled with ^{99m}Tc according to the previous work.[33] Single photon emission computed tomography/computed tomography images of two groups of BALB/c nude mice were captured at different time points after intravenously delivering the NP-FA and nanoparticles, respectively. The radioactivity of heart was determined to monitor the signal of blood by PMOD software, and the blood residence time was fitted with a one-compartment model by GraphPad software.

Animal Tumor Model and In Vivo Imaging: The tumor models were established upon subcutaneous or intraperitoneal injections of LS180 cells (≈5×10^6) into 4 weeks old male BALB/c nude mice. The tumor imaging studies were carried out 5–7 d after the inoculation of tumor cells.

The up- and down-conversion luminescence images of nude mice bearing subcutaneous and intraperitoneal tumors were acquired with IVIS Spectrum in vivo imaging system (PerkinElmer Inc., Waltham, Massachusetts) and NIR II Imaging System (Serious II 900-1700) manufactured by Suzhou NIR-Optics Co., Ltd. (China). In detail, the nude mice were anesthetized, and then the nanoprobes were intravenously injected through tail vein (15 mg of Er^{3+} per kilogram body weight), while the same dose of mother PEGylated particles were intravenously injected in another mouse as the control. For up-conversion luminescence imaging, the excitation light of 980 nm (100 mW cm^{-2}) pulsed laser was adopted, while a narrow bandpass filter of 650–690 nm (OD4) was used for collecting the emission centered at 655 nm, and the exposure time was set as 100 s. For NIR II down-conversion luminescence imaging, the excitation light of 808 nm (50 mW cm^{-2}) CW laser was used, and a long-pass filter of 1250 nm (OD4) was used for collecting the NIR II signal. The exposure time was set as 200 ms. After imaging experiments,

the mice were sacrificed, and the major organs including tumors were harvested for ex vivo imaging. The major organs and tissues including liver, spleen, kidney, heart, lung, stomach, intestine, and tumor were also collected, weighed, dissected, and eroded with concentrated nitric acid and H_2O_2 for disclosing the biodistributions of the particles by ICP-AES at 24 h postinjection.

Histochemical and Immunohistochemical Study: Adjacent slices of the intraperitoneal tumor harvested after in vivo imaging studies were prepared. The first one was stained with H&E following the standard protocol. The second one was incubated with antivimentin antibody for EMT processes tracing. The third one was incubated with anti-FR for measure the expression of FR. Specifically, formalin-fixed and paraffin-embedded tissue slices were deparaffinized and hydrated, and antigen retrieval was performed in citrate buffer (pH = 6.0). Then, endogenous peroxidase was inactivated with 3% hydrogen peroxide in methanol for 15 min, followed by incubation with bovine serum albumin to block nonspecific staining. Anti-FR or antivimentin antibody were then incubated with the slices overnight at 4 °C, after washing, the slices were treated with horseradish peroxidase-conjugated secondary antibody. After being stained with the diaminobenzidine kit, the cell nuclei were counterstained with hematoxylin. Finally, the stained slices were imaged with a microscopy.

Major organs of a group of mice ($n = 3$), including the heart, kidney, liver, lung, and spleen, were extracted 30 d postinjection of NP-FA, sectioned into thin slices, and stained with H&E for histological analysis. The control group of mice was treated with the same volume of 1 × PBS.

All animal experiments reported herein were carried out according to a protocol approved by Peking University Institutional Animal Care and Use Committee.

Supporting Information

Supporting Information is available from the Wiley Online Library or from the author.

Acknowledgements

Y.L. and P.Z. contributed equally to this work. The authors thank the financial support from the National Key Research and Development Program of China (No. 2018YFA0208800) and National Natural Science Foundation of China (NSFC) (Nos. 81771902, 81720108024, 81671754, 81530057, and 81671755), CAS-VPST Silk Road Science Fund 2019 (No. GJHZ201963), the Youth Innovation Promotion Association CAS (No. 2018042), State Key Laboratory of Luminescence and Applications (No. SKLA-2019-01).

Conflict of Interest

The authors declare no conflict of interest.

Keywords

biodistribution of folate receptors, high efficient NIR II luminescence, spatial-separation of emitting/sensitizing ions, up- and down-conversion emission imaging

Received: September 19, 2019
Revised: October 26, 2019
Published online: November 25, 2019

[1] B. Zhang, B. A. Pinsky, J. S. Ananta, S. Zhao, S. Arulkumar, H. Wan, M. K. Sahoo, J. Abeynayake, J. J. Waggoner, C. Hopes, M. J. Tang, H. J. Dai, *Nat. Med.* **2017**, *23*, 548.

[2] a) A. M. Smith, M. C. Mancini, S. Nie, *Nat. Nanotechnol.* **2009**, *4*, 710; b) C. Li, Q. Wang, *ACS Nano* **2018**, *12*, 9654.

[3] R. Weissleder, *Nat. Biotechnol.* **2001**, *19*, 316.

[4] a) A. L. Antaris, H. Chen, K. Cheng, Y. Sun, G. Hong, C. Qu, S. Diao, Z. Deng, X. Hu, B. Zhang, X. Zhang, O. K. Yaghi, Z. R. Alamparambil, X. Hong, Z. Cheng, H. Dai, *Nat. Mater.* **2016**, *15*, 235; b) H. Wan, J. Yue, S. Zhu, T. Uno, X. Zhang, Q. Yang, K. Yu, G. Hong, J. Wang, L. Li, Z. Ma, H. Gao, Y. Zhong, J. Su, A. L. Antaris, Y. Xia, J. Luo, Y. Liang, H. Dai, *Nat. Commun.* **2018**, *9*, 1171.

[5] a) O. T. Bruns, T. S. Bischof, D. K. Harris, D. Franke, Y. Shi, L. Riedemann, A. Bartelt, F. B. Jaworski, J. A. Carr, C. J. Rowlands, M. W. B. Wilson, O. Chen, H. Wei, G. W. Hwang, D. M. Montana, I. Coropceanu, O. B. Achorn, J. Kloepper, J. Heeren, P. T. C. So, D. Fukumura, K. F. Jensen, R. K. Jain, M. G. Bawendi, *Nat. Biomed. Eng.* **2017**, *1*, 0056; b) K. J. McHugh, L. Jing, A. M. Behrens, S. Jayawardena, W. Tang, M. Gao, R. Langer, A. Jaklenec, *Adv. Mater.* **2018**, *30*, 1706356; c) B. Dong, C. Li, G. Chen, Y. Zhang, Y. Zhang, M. Deng, Q. Wang, *Chem. Mater.* **2013**, *25*, 2503; d) G. Hong, J. T. Robinson, Y. Zhang, S. Diao, A. L. Antaris, Q. Wang, H. Dai, *Angew. Chem., Int. Ed.* **2012**, *51*, 9818.

[6] a) G. Hong, J. C. Lee, J. T. Robinson, U. Raaz, L. Xie, N. F. Huang, J. P. Cooke, H. Dai, *Nat. Med.* **2012**, *18*, 1841; b) G. Hong, S. Diao, J. Chang, A. L. Antaris, C. Chen, B. Zhang, S. Zhao, D. N. Atochin, P. L. Huang, K. I. Andreasson, C. J. Kuo, H. Dai, *Nat. Photonics* **2014**, *8*, 723.

[7] J. Qi, C. Sun, D. Li, H. Zhang, W. Yu, A. Zebibula, J. W. Y. Lam, W. Xi, L. Zhu, F. Cai, P. Wei, C. Zhu, R. T. K. Kwok, L. L. Streich, R. Prevedel, J. Qian, B. Z. Tang, *ACS Nano* **2018**, *12*, 7936.

[8] J. Zhou, Y. Jiang, S. Hou, P. K. Upputuri, D. Wu, J. Li, P. Wang, X. Zhen, M. Pramanik, K. Pu, H. Duan, *ACS Nano* **2018**, *12*, 2643.

[9] a) Y. Zhong, Z. Ma, S. Zhu, J. Yue, M. Zhang, A. L. Antaris, J. Yuan, R. Cui, H. Wan, Y. Zhou, W. Wang, N. F. Huang, J. Luo, Z. Hu, H. Dai, *Nat. Commun.* **2017**, *8*, 737; b) Y. Fan, P. Wang, Y. Lu, R. Wang, L. Zhou, X. Zheng, X. Li, J. A. Piper, F. Zhang, *Nat. Nanotechnol.* **2018**, *13*, 941.

[10] a) D. J. Naczynski, M. C. Tan, M. Zevon, B. Wall, J. Kohl, A. Kulesa, S. Chen, C. M. Roth, R. E. Riman, P. V. Moghe, *Nat. Commun.* **2013**, *4*, 2199; b) C. Liu, Y. Hou, M. Gao, *Adv. Mater.* **2014**, *26*, 6922.

[11] a) G. Chen, T. Y. Ohulchanskyy, S. Liu, W. C. Law, F. Wu, M. T. Swihart, H. Agren, P. N. Prasad, *ACS Nano* **2012**, *6*, 2969; b) I. Villa, A. Vedda, I. X. Cantarelli, M. Pedroni, F. Piccinelli, M. Bettinelli, A. Speghini, M. Quintanilla, F. Vetrone, U. Rocha, C. Jacinto, E. Carrasco, F. S. Rodríguez, Á. Juarranz, B. del Rosal, D. H. Ortgies, P. H. Gonzalez, J. G. Solé, D. J. García, *Nano Res.* **2014**, *8*, 649.

[12] F. Ren, L. Ding, H. Liu, Q. Huang, H. Zhang, L. Zhang, J. Zeng, Q. Sun, Z. Li, M. Gao, *Biomaterials* **2018**, *175*, 30.

[13] S. Diao, G. Hong, A. L. Antaris, J. L. Blackburn, K. Cheng, Z. Cheng, H. Dai, *Nano Res.* **2015**, *8*, 3027.

[14] W. You, D. Tu, W. Zheng, X. Shang, X. Song, S. Zhou, Y. Liu, R. Li, X. Chen, *Nanoscale* **2018**, *10*, 11477.

[15] R. Qiao, C. Liu, M. Liu, H. Hu, C. Liu, Y. Hou, K. Wu, Y. Lin, J. Liang, M. Gao, *ACS Nano* **2015**, *9*, 2120.

[16] a) F. Wang, X. Liu, *Chem. Soc. Rev.* **2009**, *38*, 976; b) M. Haase, H. Schafer, *Angew. Chem., Int. Ed.* **2011**, *50*, 5808.

[17] S. Wen, J. Zhou, K. Zheng, A. Bednarkiewicz, X. Liu, D. Jin, *Nat. Commun.* **2018**, *9*, 2415.

[18] N. J. Johnson, S. He, S. Diao, E. M. Chan, H. Dai, A. Almutairi, *J. Am. Chem. Soc.* **2017**, *139*, 3275.

[19] a) M. Jiang, H. Liu, S. Zeng, J. Hao, *Adv. Therap.* **2019**, *2*, 1800153; b) Y. Li, S. Zeng, J. Hao, *ACS Nano* **2019**, *13*, 248.

[20] a) C. Liu, Z. Gao, J. Zeng, Y. Hou, F. Fang, Y. Li, R. Qiao, L. Shen, H. Lei, W. Yang, M. Gao, *ACS Nano* **2013**, *7*, 7227; b) C. Liu, Y. Qi,

R. Qiao, Y. Hou, K. Chan, Z. Li, J. Huang, L. Jing, J. Du, M. Gao, *Nanoscale* **2016**, *8*, 12579.
[21] Q. Chen, X. Xie, B. Huang, L. Liang, S. Han, Z. Yi, Y. Wang, Y. Li, D. Fan, L. Huang, X. Liu, *Angew. Chem., Int. Ed.* **2017**, *56*, 7605.
[22] L. Tu, X. Liu, F. Wu, H. Zhang, *Chem. Soc. Rev.* **2015**, *44*, 1331.
[23] F. Wang, J. Wang, X. Liu, *Angew. Chem., Int. Ed.* **2010**, *49*, 7456.
[24] S. Fischer, N. D. Bronstein, J. K. Swabeck, E. M. Chan, A. P. Alivisatos, *Nano Lett.* **2016**, *16*, 7241.
[25] X. Sun, B. Wang, I. Kempson, C. Liu, Y. Hou, M. Gao, *Small* **2014**, *10*, 4711.
[26] X. Lei, R. Li, D. Tu, X. Shang, Y. Liu, W. You, C. Sun, F. Zhang, X. Chen, *Chem. Sci.* **2018**, *9*, 4682.
[27] C. Wurth, S. Fischer, B. Grauel, A. P. Alivisatos, U. Resch-Genger, *J. Am. Chem. Soc.* **2018**, *140*, 4922.
[28] a) R. Qiao, H. Qiao, Y. Zhang, Y. Wang, C. Chi, J. Tian, L. Zhang, F. Cao, M. Gao, *ACS Nano* **2017**, *11*, 1816; b) S. Qiu, J. Zeng, Y. Hou, L. Chen, J. Ge, L. Wen, C. Liu, Y. Zhang, R. Zhu, M. Gao, *Nanoscale* **2018**, *10*, 21772; c) P. Zhang, Y. Hou, J. Zeng, Y. Li, Z. Wang, R. Zhu, T. Ma, M. Gao, *Angew. Chem., Int. Ed.* **2019**, *58*, 11088.
[29] a) L. Ma, Y. Liu, L. Liu, A. Jiang, F. Mao, D. Liu, L. Wang, J. Zhou, *Adv. Funct. Mater.* **2018**, *28*, 1705057; b) X. Wang, A. Yakovliev, T. Y. Ohulchanskyy, L. Wu, S. Zeng, X. Han, J. Qu, G. Chen, *Adv. Opt. Mater.* **2018**, *6*, 1800690.
[30] Y. Hou, R. Qiao, F. Fang, X. Wang, C. Dong, K. Liu, C. Liu, Z. Liu, H. Lei, F. Wang, M. Gao, *ACS Nano* **2013**, *7*, 330.
[31] M. Jiao, L. Jing, C. Liu, Y. Hou, J. Huang, X. Wei, M. Gao, *Chem. Commun.* **2016**, *52*, 5872.
[32] a) J. Shia, D. S. Klimstra, J. R. Nitzkorski, P. S. Low, M. Gonen, R. Landmann, M. R. Weiser, W. A. Franklin, F. G. Prendergast, L. Murphy, L. H. Tang, L. Temple, J. G. Guillem, W. D. Wong, P. B. Paty, *Hum. Pathol.* **2008**, *39*, 498; b) G. Toffoli, C. Cernigoi, A. Russo, A. Gallo, M. Bagnoli, M. Boiocchi, *Int. J. Cancer* **1997**, *74*, 193.
[33] Z. Gao, Y. Hou, J. Zeng, L. Chen, C. Liu, W. Yang, M. Gao, *Adv. Mater.* **2017**, *29*, 1701095.

